The iron brain: Post-mortem and in vivo imaging of iron in brain diseases

Bulk, M.

3

Post-Mortem MRI and histology demonstrate differential iron accumulation and cortical myelin organization in early and late onset Alzheimer's disease

This chapter has been published as *Neurobiology of Aging* **62**, 231 (2018)

Marjolein Bulk*
Walid M. Abdelmoula*
Rob J.A. Nabuurs
Linda M. van der Graaf
Coen W.H. Mulders
Aat A. Mulder
Carolina R. Jost
Abraham J. Koster
Mark A. van Buchem
Remco Natté
Jouke Dijkstra
Louise van der Weerd

*These authors contributed equally to this study

ABSTRACT

Previous MRI studies reported cortical iron-accumulation in early-onset (EOAD) compared to late-onset (LOAD) Alzheimer patients. However, the pattern and origin of iron accumulation is poorly understood. This study investigated the histopathological correlates of MRI contrast in both EOAD and LOAD. T_2^*-weighted MRI was performed on post-mortem frontal cortex of controls, EOAD, and LOAD. Images were ordinally scored using predefined criteria followed by histology. Non-linear histology-MRI registration was used to calculate pixel-wise spatial correlations based on the signal intensity. EOAD and LOAD were distinguishable based on 7T MRI from controls and from each other. Histology-MRI correlation analysis of the pixel intensities showed that the MRI contrast is best explained by increased iron accumulation and changes in cortical myelin, whereas amyloid and tau showed less spatial correspondence with T_2^*-weighted MRI. Neuropathologically, sub-types of Alzheimer's disease showed different patterns of iron accumulation and cortical myelin changes independent of amyloid and tau that may be detected by high-field susceptibility-based MRI.

3.1. INTRODUCTION

Alzheimer's disease (AD) is a neurodegenerative disease and the most frequent cause of dementia [1]. AD is typically associated with age, however in 1-5% of the patients the disease develops before the age of 65, often referred to as early-onset AD (EOAD) [1, 2]. Patients with familial AD often present with an early-onset, but only a small proportion of all EOAD cases is caused by an autosomal dominant mutation in the PSEN1, PSEN2 or APP gene. In contrast, in late-onset AD (LOAD) the APOE-ϵ4 allele is the most important genetic factor [3]. Apart from genetic differences, previous studies reported differences in cognitive impairment profiles, a more rapid cognitive decline [4, 5], and a more severe post-mortem pathology in EOAD patients [6, 7].

The pathophysiology of AD is still incompletely understood and non-invasive methods to detect AD in vivo at an early stage are important to increase our understanding of the disease. Presently, the clinical diagnosis AD is based on medical and family history and loss of performance in certain cognitive domains [3]. Additional support for the diagnosis is based on the presence and levels of amyloid beta ($A\beta$) 1-40/1-42 peptides, modified and total tau proteins in CSF and information from PET, MRI, or other imaging methods [3, 8, 9]. However, the definitive diagnosis of AD can still only be made post-mortem, as histological confirmation of the presence of $A\beta$ plaques and neurofibrillary tangles is required [3, 10].

Although $A\beta$ and hyper phosphorylated tau are still considered key mediators in AD pathogenesis, an increasing number of studies suggest that changes in iron metabolism might also play a role [11–13]. In AD and other neurodegenerative diseases, iron accumulation has been shown to affect the progression of neurodegeneration through several mechanisms. A well-known consequence of increased iron in neurodegenerative diseases is the production of reactive oxygen species (ROS), leading to DNA damage and cell death [14]. Additionally, amyloid cleavage and clearance and intracellular iron storage and clearance are regulated by several common pathways. Two of these are firstly the furin activation pathway, which regulates both secretase-mediated APP cleavage and intracellular iron uptake [15]. Secondly, APOE -mediated lipid transport is involved in clearance of both $A\beta$ and iron, with APOE -ϵ4 showing reduced clearance due to its low affinity for high-density lipoprotein [16]. Furthermore, mutations in iron-regulating proteins, such as transferrin and human hemochromatosis protein (HFE), have a higher incidence in AD patients, stressing the interaction between iron and AD pathogenesis [17].

Previous *ex vivo* studies, using high-field T_2^*-weighted MRI sequences, which are highly sensitive for iron deposits in the brain, reported iron-induced intensity changes in the cortex of post-mortem brain tissue of patients with AD. In these studies both hypointense foci [18–20] and inhomogeneous cortices [19] were found on T_2^*-weighted images of post-mortem AD brain tissue. Histological comparison revealed

co-localization with iron and partial co-localization with $A\beta$ plaques [18–20]. More recent in vivo 7T MRI studies reported cortical iron accumulation in AD patients [21] and PiB-positive mild cognitive impairment subjects [22]. Moreover, another in vivo 7T MRI study reported cortical phase differences between EOAD and LOAD patients. This study suggests that EOAD patients have an increased iron accumulation in specific cortical areas, as for example the middle frontal gyrus, compared to LOAD patients [23]. Despite these previous studies, the exact pattern of iron accumulation and the co-localization with specific cells and AD biomarkers is poorly understood.

Therefore, the objective of this study was to gain more insight into the histopathological correlates of the observed T_2^*-weighted contrast changes in AD and to further investigate the presence of iron in both LOAD and EOAD. We performed ultra-high field ex vivo MRI and histopathological examination on post-mortem tissue blocks of the frontal cortex of both LOAD and EOAD patients. Pixel-by-pixel correlation analysis was done after non-linear histology-MRI registration to find the histological correlates of MRI contrast.

3.2. METHODS

3.2.1. POST-MORTEM BRAIN MATERIAL

To investigate the histopathological correlates of the observed T_2^*-weighted contrast changes, post-mortem brain samples of the frontal lobe were obtained of 13 control subjects, 10 LOAD patients, and 11 EOAD patients from the Netherlands Brain Bank and the Normal Aging Brain Collection (Table 3.1).

Based on a previous study by van Rooden et al., 2015, tissue blocks of the middle frontal gyrus were selected [23]. Tissue was fixed in 4% phosphate buffered formalin and to avoid formalin-induced artefacts on MRI, only material fixed for a maximum period of three years was selected [24]. All tissue blocks were fixed for a minimum of four weeks and a maximum of three years, in most cases not more than one year for both control subjects and AD patients. No significant difference in these factors was found between control subjects, LOAD, and EOAD patients.

From each subject one tissue block of approximately 20x15x15 mm was resected and placed individually in a regular 15 ml tube (Greiner Bio-One). To partially restore MR relaxation parameters residual formalin was removed by washing the tissue block in phosphate buffered saline (PBS) for > 24 hours [25]. Before MRI, the 15 ml tube containing the tissue block was filled with a proton-free fluid (Fomblin LC08, Solvay). Care was taken to avoid the inclusion of trapped air bubbles.

For two EOAD patients a frozen tissue block of the middle frontal gyrus was obtained from the Netherlands Brain Bank to investigate the effect of prolonged formalin storage

	Controls (n=13)	LOAD (n=10)	EOAD (n=11)
Mean age of onset, y (range)	-	79,4 (69-89)	52,5 (34-64)++
Mean age of death, y (range)	80,2 (64-93)	85,8 (73-96)	67,3 (43-91) *,++
Male/female	5/8	4/6	4/7
Braak, median (range)	2 (0-3)	5 (4-6) **	6 (4-6) **
APOE- ϵ4 carriers	1/8	8/10*	5/11
Genetic mutation (number of known cases)	Unknown	Unknown	APP (1), PSEN1 (1)
$A\beta$ load, median (range)	1 (0-2)	3 (2-3) **	3 (3) **
Tau load, median (range)	0 (0-1)	2 (1-3) **	4 (3-4) **, ++
Post-mortem interval, mean (sd)	6h:39m (1h:21m)	5h:17m (1h:20m)*	5h:01m (1h:02m)*
Duration formalin-fixation, median (range)	1 year (0-3)	1 year (0-3)	1 year (0-3)

Table 3.1: **Case characteristics and histopathological findings.** * Indicates a significant difference between controls and LOAD and/or controls and EOAD patients. + Indicates a significant difference between LOAD and EOAD patients. */+ indicates $p < 0.05$ and **/++ indicates $p < 0.001$.
Note: APOE- ϵ4 = Apolipoprotein E ϵ4 gene allele, EOAD = Early- onset Alzheimer's Disease patients, LOAD = Late- onset Alzheimer's Disease patients.

on MRI. This deeply frozen tissue block was thawed in formalin and fixed for three days at room temperature. After three days, the same protocol was followed as for the formalin-fixed tissue blocks; the MR relaxation parameters were partially restored by immersing the tissue block in PBS for > 24 hours. Before MRI, the 15 ml tube containing the tissue block was filled with a proton-free fluid (Fomblin LC08, Solvay). Care was taken to avoid the inclusion of trapped air bubbles.

3.2.2. POST-MORTEM MRI ACQUISITION AND ANALYSIS

Multiple Gradient Echo scans with a total imaging time of 210 minutes were acquired from each brain sample on a 7T horizontal bore Bruker MRI system (Bruker Biospin, Ettlingen, Germany). The third echo (TE 33.9 ms) was selected because these magnitude images had the best contrast compared to the other echoes, based also on a previous publication [19]. Pre-defined scoring criteria which were based on a previous 7T MRI study of the human cortex to define normal and abnormal cortex were used [19].

The previously used scoring criteria (e.g. homogeneity of the cortex) was extended with the presence of a diffuse hypointense band which was clearly observed due to high-spatial-resolution in these post-mortem scans.

A normal cortex was defined as either a cortex containing one homogeneous layer with a higher signal intensity compared to the adjacent white matter, or a homogeneous cortex containing two or three homogeneous, well-defined layers observed as normal cortical lamination (Fig. 3.1A). The superficial layer has a higher signal intensity compared to the deepest layers. The same layers as previously described are present in the cortex with three layers, but separated by a third thin layer with a lower signal intensity compared to the other layers, as described previously in cortical regions with highly myelinated layers (e.g. the line of Baillarger) [26]. In a normal cortex with normal cor-

Criteria	Scoring	Value
Homogeneity of the cortex	Yes (homogeneous) No (inhomogeneous)	0 2
Diffuse hypointense band (arrows)	Present Partially present Absent	2 1 0

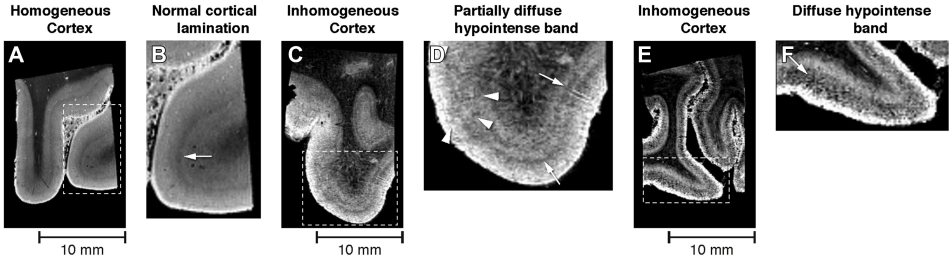

Figure 3.1: **MRI scoring criteria, corresponding values and imaging examples.** (A) A normal cortex was defined as a homogeneous cortex with one to three homogenous well-defined layers, including normal cortical lamination (B, arrow). (C,E) An abnormal cortex was defined as an inhomogeneous cortex with a granular and/or patchy structure and foci of signal loss. (F, arrow) In addition, diffuse areas of lower signal intensity covering the middle cortical layers obscuring the normal cortical lamination was defined as a diffuse hypointense band. (D) In case of a partially present diffuse hypointense band, these areas of lower signal intensities were only weakly or intermittently observed throughout the cortical ribbon. For example in D, in the same cortical ribbon both normal cortical lamination (arrows) as areas of lower signal intensity could be observed (arrow heads). A total score was calculated from the values of each criteria, with a minimum score of 0/4 indicating a normal cortex and a maximum of 4/4 indicating an abnormal cortex.

tical lamination, no diffuse hypointense band was observed (Fig. 3.1B, arrow).

An abnormal cortex was defined as a cortex with a granular/patchy structure containing foci of signal loss and one inhomogeneous layer with loss of normal cortical lamination (e.g. without two or three well-defined layers) (Fig. 3.1C,E). Diffuse areas of lower signal intensity covering the middle cortical layers obscuring the normal cortical lamination was defined as a diffuse hypointense band (Fig. 3.1F, arrow).

All images were scored for absence or presence of above mentioned criteria. As shown in Fig. 3.1, different scoring values were used per criteria to indicate presence, partially presence or absence of the criteria. A weakly or intermittently observed diffuse hypointense band throughout the cortical ribbon was scored as partially present (Fig. 3.1D, arrows). A total score was calculated from the values of each criteria, with a minimum score of 0/4 indicating a normal cortex and a maximum of 4/4 indicating an abnormal cortex. Window settings were standardized for each image and all scans were scored by two independent blinded trained observers. Agreement values were calculated and consensus was reached in all cases of disagreement.

3.2.3. HISTOLOGY AND IMMUNOHISTOCHEMISTRY

The same brain samples as used for MRI were used for histology. Tissue blocks were embedded in paraffin and serially cut into 8 μm and 20 μm thick sections. A 20 μm thick section was used for histochemical iron detection according to Meguro et al. [27, 28]. Another 20 μm thick section was used for immunohistemical detection of myelin, and the 8 μm sections were stained for $A\beta$, paired helical filament-tau, microglia and activated astrocytes (Suppl. Table 1). Primary antibodies were incubated overnight at room temperature, followed by the secondary antibody and avidin-biotin complex (ABC, Vector Labs, CA, USA). Signal enhancement was completed by immersion in DAB. The 8 μm sections were counterstained with Harris Haematoxylin. Semi-quantitative histological analysis was done to assess the pathological burden of amyloid, tau, iron and myelin.

3.2.4. HISTOLOGY-MRI REGISTRATION

Registration of all histological images to the corresponding MRI images was done to determine which staining correlated best with the MRI image. To facilitate their comparison, histological images were first pre-processed and then non-linearly aligned to the corresponding MR image. Briefly, all digitized histological images were first pre-processed to exclude the background noise. The high resolution histological images were processed using the pre-processing pipeline proposed by Abdelmoula et al [29]. After pre-processing, the high resolution histological images were down-sized to the same range of the MRI image size, facilitating the registration initialization [30].

The most similar MRI slice with respect to the given histology was selected based on the physical location of the section in the tissue block, measured by counting the number of sections taken starting at the block surface. At this approximate location, the most similar MRI slice was chosen by visual comparing clearly detectable landmarks (contours, vasculature, tears etc.). Due to manually selecting the most similar MRI slice, minor changes in tilt were not accounted for. In each MRI slice the cortex including all cortical layers was manually annotated by a trained observer (MB), and used as region of interest for correlation analysis.

Non-linear registration was performed to align the manually selected 2D MRI and histological images. The parametric-based registration scheme was used in which B-Spline transformation was chosen to correct for local deformations and the cost function of mutual information was used to assess the quality of multi-modal registration. The registration results were qualitatively quantified by visual inspection of superimposing the reference and the aligned images on top of each other. Smooth transitions between same structures in different images mean a good registration has been achieved.

After registration, the regions of interest were projected on each of the aligned histological images. Visual examination confirmed the quality of ROIs propagation on top of the aligned histology. Pixel-based spatial correlations of the signal intensities were computed within that annotated region for each histological image and the corresponding MR image.

3.2.5. SI MATERIALS AND METHODS

Detailed descriptions of the post-mortem tissue samples, post-mortem MRI acquisition and analysis, histology and histological analysis, electron microscopy, histology-MRI registration, and statistics are provided in SI Appendix, Materials and Methods at the end of this chapter.

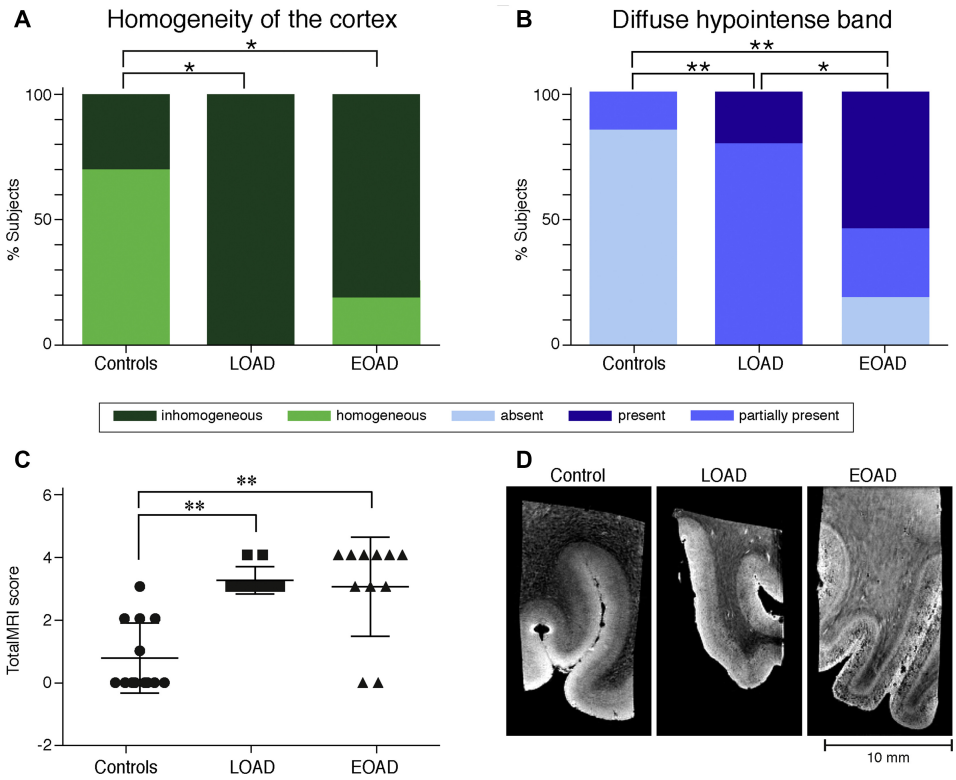

Figure 3.2: **Results MRI scores and representative MRI images.** (A) An inhomogeneous cortex was more frequently found in both AD groups. (B) In addition, a diffuse hypointense band was more frequently found in AD patients, especially in the EOAD patients. (C) Both AD groups had a significantly higher mean total MRI score, indicating that both AD groups had an abnormal cortical appearance on MRI compared to control subjects. (D) Representative MRI images show that AD patients have a different cortical appearance compared to controls, characterized by inhomogeneities and a diffuse hypointense band covering the central layers of the cortex. Overall, EOAD patients were more affected on MRI compared to LOAD patients.

3.3. RESULTS

3.3.1. AD PATIENTS HAVE A DIFFERENT CORTICAL APPEARANCE ON T_2^* WEIGHTED MRI

Previous in vivo imaging studies already showed that cortical susceptibility-based contrast is observed in AD patients. To assess these differences in cortical appearance in post-mortem tissue of control subjects, LOAD and EOAD patients, MRI scans of tissue blocks of the frontal cortex were scored for predefined criteria (Fig. 3.1) by two independent blinded observers. The κ value for interobserver agreement was substantial for homogeneity of the cortex ($\kappa = 0.73$) and diffuse hypointense band ($\kappa = 0.70$).

An inhomogeneous cortex, observed as a cortex with a granular and/or patchy struc-

ture containing foci of signal loss (Fig. 3.1C,E, 3.2A), was frequently observed in both LOAD and EOAD patients (19/21 cases). In contrast, only three out of 13 control subjects were scored as inhomogeneous. In addition, we observed a hypointense diffuse band-shaped area of signal loss with a grainy appearance covering the middle layers of the cortex (described as a diffuse hypointense band in the rest of the text). This diffuse hypointense band was present or partially present in all LOAD and 9/11 EOAD patients, whereas in only two control subjects this band was partially observed (2/13 cases (Fig. 3.2B)). Overall, the diffuse hypointense band was most striking in the EOAD patients.

To differentiate between a normally-appearing and abnormally-appearing cortex, the individual criteria were summed up to calculate a total MRI score with a minimum score of 0/ 4 and a maximum score of 4/4. Both LOAD and EOAD patients had a significantly higher mean total MRI score, indicating that both AD groups have an abnormal cortical appearance on MRI compared to control subjects (Fig. 3.2C). Figure 3.2D shows representative MR images of a cortex from a normal control cortex (total score of 0), a cortex from a LOAD patient (total score of 3), and an EOAD patient (total score of 4). As can been seen from these results (Fig. 3.2C,D), AD patients have a different cortical appearance compared to control subjects, characterized by inhomogeneities, and a diffuse hypointense band covering the central layers of the frontal cortex. In addition, the EOAD patients were generally more affected on MRI compared to LOAD patients.

3.3.2. HISTOPATHOLOGICAL ASSESSMENT OF $A\beta$, TAU, MYELIN, AND IRON

After MRI, all tissue blocks were processed for histological analysis and the pathological burden was assessed for all subjects by two independent blinded observers (Table 3.1). The majority of the AD patients showed high $A\beta$ plaque load (18/21 cases) and some control subjects showed a low to moderate amount of $A\beta$ plaques (7/13 cases). Neurofibrillary degeneration, in the form of hyperphosphorylated tau in neuronal cell bodies and processes, was found in all AD patients and in one control. In general, EOAD patients were more affected than LOAD patients.

Myelin and iron stainings were also performed since both are potential sources of T_2^*-weighted MRI contrast. Histopathological assessment showed a normal myelin distribution in all control subjects and nearly all LOAD patients with the typical increased staining intensity in myelin rich areas including the white matter (WM), the lines of Baillarger and the myelinated fiber bundles formed by pyramidal cell output axons traversing from the WM into the cortex (Fig. 3.3B1). In contrast, only three EOAD patients showed a normal appearance of cortical myelin. The other patients had a diffuse band-shaped increased myelin staining covering the middle layers of the cortex (III/IV), sometimes extending to layer II and V (Fig. 3.3B2). This diffuse band-shaped increased myelin staining intensity disturbed the normal lines of Baillarger and was

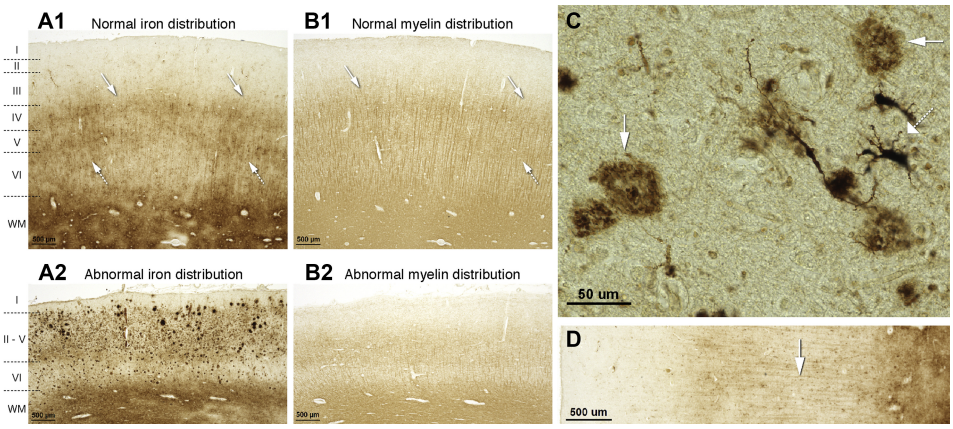

Figure 3.3: **Normal and abnormal cortical iron and myelin distribution.** (A1) A normal myelin-associated increased iron staining was found in the WM, lines of Baillarger (arrows) and fibers transversing into the GM. (B1) Normal myelin distribution was observed as an increased staining intensity in myelin-rich areas including the WM, the lines of Baillarger (arrows) and in fibers projecting from the WM into the cortex. (A2, B2) Abnormal iron and myelin was observed as a diffuse band-shaped increased staining intensity covering the middle cortical layers (III/IV), extending till layer II and V. (C, D) In addition, the iron staining showed focal iron accumulation in $A\beta$ plaques (C, arrow), microglia (C, dotted arrow) and myelin fibers (D, arrow). Please note that the cortex is clearly thinner in the EOAD subject presented in A2 and B2, due to cortical atrophy.

observed in eight out of 13 EOAD patients and one LOAD patient.

In normal control cortex iron was concentrated in the myelin rich areas of the WM, the lines of Baillarger and myelinated fibers traversing from the WM into the cortex (Fig. 3.3A1). In AD patients iron accumulated on a subset of $A\beta$ plaques, microglia and, as observed in control subjects, in areas with increased myelin (Fig. 3.3C,D). In addition, in 3/8 LOAD and 6/10 EOAD patients an altered pattern of diffuse myelin associated iron accumulation was observed (Fig. 3.3A2). In these patients, abnormal cortical iron was observed as a diffuse band-shaped pattern of increased myelin associated iron covering the middle layers of the cortex (III/IV), sometimes extending till layer II and V, obscuring the lines of Baillarger (Fig. 3.3A2). In two control subjects and three AD patients the iron staining showed artefacts and these subjects were therefore not examined.

3.3.3. MRI CONTRAST IN AD IS MAINLY IRON AND MYELIN DRIVEN

Comparing the histological images with the MRI images already suggested that the differences found on MRI mainly co-localize with changes in iron and myelin organization (Fig. 3.4). To quantify this finding, non-linear histology-MRI registration was performed followed by spatial correlation analysis of the cortical pixel intensities.

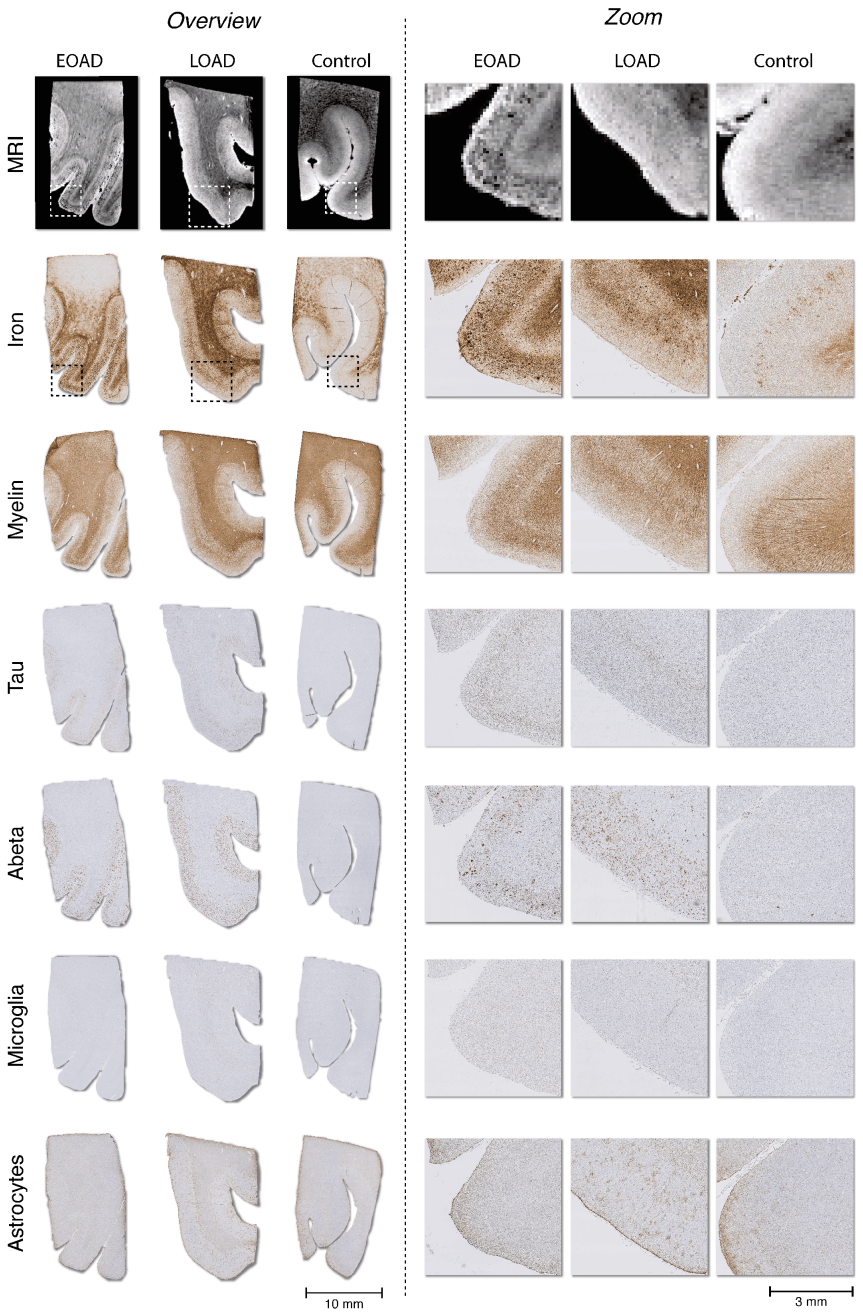

Figure 3.4: **MRI and histology of a control, LOAD and EOAD patient.** Overview and zoomed images (indicated with a box) of both MRI and histology are presented. Comparing the histological images with the MRI images suggested that the differences found on MRI mainly co-localize with changes in iron and myelin organization in all three groups. Due to resolution, the relatively sparse and small microglia are not visible in this figure, however, microglia were observed in all subjects. A representative high-resolution zoomed image of microglia in the cortex is shown in Suppl. Fig. S3.

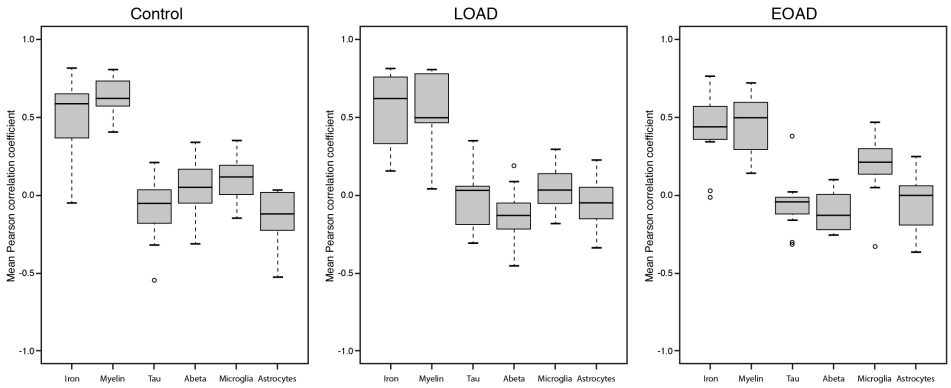

Figure 3.5: **Histology- MRI correlation analysis of the cortical pixel intensities.** A high spatial correlation was found for the iron and myelin staining. Less spatial correlation was found for the $A\beta$, tau, microglia and astrocyte staining.

In both control subjects and AD patients, a significant high spatial correlation was found between the MRI image intensity and the iron and myelin staining intensity (Fig. 3.5). Less spatial correlation was found for the $A\beta$, tau, microglia and astrocyte staining. Although differences were found in severity of $A\beta$ and tau pathology between control subjects and AD patients, no difference was found in the correlation analyses; both the control and AD groups showed low spatial correlation between MRI and $A\beta$ and/or tau. Only in EOAD patients the microglia staining showed a higher spatial correlation compared to the $A\beta$, tau and astrocyte staining, suggesting that microglia might be a contributing factor to the observed contrast changes in EOAD patients.

3.3.4. CORTICAL MYELIN ORGANIZATION IS CHANGED IN AD

Apart from the iron staining, also the myelin staining showed a high correlation with the diffuse hypointense band on MRI. Therefore, the cortical myelin in layer IV of the frontal cortex was examined in more detail (Fig. 3.6). Microscopically, the myelin architecture in layer IV of the frontal cortex in the majority of the controls (9/13) , 3/9 LOAD patients and one EOAD patient showed the typical organized raster-like structure with myelinated fibers traversing all cortical layers, as well as fibers running parallel to the cortical surface. Structural myelin organization was scored by two observers and consensus was reached in all cases. The myelin architecture in 4/9 LOAD patients and 2/11 EOAD patients were scored as more disorganized compared to the majority of the controls , noticeable as a less clear raster-like structure and less fibers traversing all cortical layers. In the majority of the EOAD patients (8/11) and two LOAD patients the myelin architecture was scored as significantly disorganized, characterized by crowded reticular fibers and loss of raster-like organization.

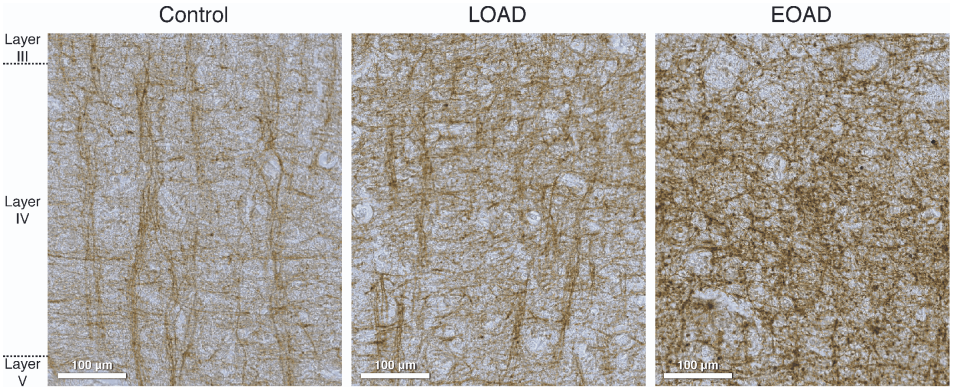

Figure 3.6: **Myelin architecture of layer IV of the frontal cortex.** Control subjects showed the typical organized, raster-like myelin architecture. LOAD patients were scored as showed more disorganization, noticeable as a less clear raster-like structure and less fibers traversing all cortical layers. In contrast, the myelin architecture of EOAD patients was scored as significantly disorganized, characterized by crowded reticular fibers and loss of raster-like organization.

3.3.5. ULTRASTRUCTURAL LOCALIZATION OF IRON IN MYELIN

The increased myelin associated iron in AD patients suggested a change in cortical iron accumulation and prompted us to further investigate the location of iron at the ultrastructural level in one control and one EOAD patient. Using electron microscopy, we further investigated where iron was located, i.e. within the myelin sheaths, nuclei or neuropil. Additionally, we identified iron-accumulating cells to further confirm our histological observations. Electron microscopy revealed in tissue of an EOAD patient, as also stated by Quintana et al. [31], the presence of iron when splitting of adjacent myelin lamellae has taken place. Between spit lamellae one finds vacuoles that can contain remnants of cytoplasm presumably derived from the oligodendrocyte forming the sheath. Iron is found lining the vacuoles that can bulk inward towards the axon or outward towards the cytoplasm. (Fig. 3.7A, B). Iron was not found in axons without myelin splitting (Fig. 3.7C). As the tissue was not fixed with optimal protocols to prevent disruption of the myelin sheaths [32], we cannot draw conclusions on ultrastructural myelin damage in the AD patients based on this material. The procedure to detect iron results in the loss of nuclear and cytoplasmic structures. As a result the glia cannot be classified solely according to morphology. Occasionally cells are found with a process extending from this cell which is in very close proximity to a myelinated axon and seems to enwrap this axon, suggesting that these cells are oligodendrocytes [33]. We have found iron present in these cells both in the cytoplasm and the nucleus. (Fig. 3.7D). A large amount of iron is also found in cells containing inclusions (Fig. 3.7E). These inclusions are clearly the result of phagocytosis and these cells are therefore believed to be microglia [33]. Cells with the morphological traits of neurons, that have a large round nucleus and sparse heterochromatin primarily present bordering the nu-

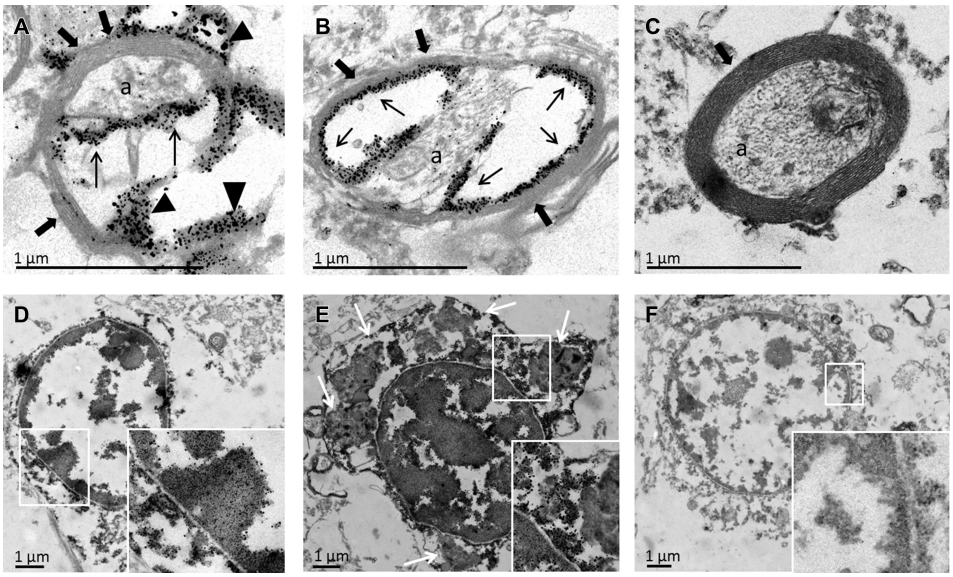

Figure 3.7: **Ultrastructural localization of iron in myelin.** Ultrastructural localization of iron amidst the myelin sheaths and in the nucleus and cytoplasm of oligodendrocytes in the cortex of an EOAD patient. (A + B) Electron microscopy showed iron accumulation between split myelin sheaths. Arrows show iron lining vacuoles resulting from split myelin sheaths with bulging of the sheath towards the flattened axon (indicated by a). Arrow heads show vacuoles bulging out toward the cytoplasm containing iron. (C) Iron was not observed in normal axons (indicated by a) without myelin splitting. (D) A nucleus of an oligodendrocyte in the cortex of an EOAD patient. Iron is clearly visible in the nucleus and cytoplasm. Inset shows iron particles in the nucleus and cytoplasm. (E) A large amount of iron is also found in cells containing inclusions (arrows) which are clearly the result of phagocytosis and these cells are therefore believed to be microglia. (F) A nucleus of a neuron as found in the cortex of an EOAD patient, no iron is found in the nucleus and cytoplasm. Inset: shows detail of the same nucleus. (A,B,C) Thick arrows indicate the myelin sheaths. The axon is indicated by a.

clear envelope show little to no iron. (Fig. 3.7F). The same is true for endothelial cells lining the blood vessels (Suppl. Fig. S4). The same locations of iron were found in control tissue. We did not describe any possible differences in myelin integrity between these two subjects, because this material was initially fixed for histology, a protocol which may disrupt the myelin sheaths, resulting in experimental artefacts resembling membrane blobbing [32].

3.3.6. CORTICAL APPEARANCE ON MRI IN TWO ATYPICAL AD CASES

As shown in Fig. 3.2C, two EOAD patients had a normal cortical appearance according the total MRI score. To confirm this finding, a MRI scan of an adjacent tissue block was made of both patients. This showed the same normal cortical appearance for both patients (Suppl. Fig. S5A,B). We hypothesised that leakage of iron due to prolonged formalin storage might be the cause of these results. Therefore we scanned a frozen tissue

block, which was thawed in formalin and fixed for three days at room temperature, of the same brain region of one patient. However, also this MRI scan showed a normal cortical appearance and thereby excluded leakage of iron as a cause (Suppl. Fig. S5C).

3.4. DISCUSSION

This study aimed to gain more insight into the histopathological correlates of the previously observed T_2^*-weighted MRI contrast changes in AD and to further investigate the presence of iron in both LOAD and EOAD. Ultra-high field MRI of post-mortem brain tissue showed that AD patients have a different cortical appearance compared to control subjects upon visual rating, characterized by inhomogeneities and a diffuse hypointense band covering the central layers of the cortex. Non-linear histology-MRI registration revealed that iron and myelin changes are the predominant source of the observed MRI contrast changes. Overall, the observed diffuse hypointense band was scored as more intense in EOAD patients compared to LOAD patients.

Previous MRI studies heavily focussed on the correlation of iron-induced contrast changes and individual $A\beta$ plaques [18–20, 34]. These studies used thin tissue sections, very high magnetic fields (9.4T), very high resolutions (40 μm^2), and it's not clear whether these results are also visible in a more clinical setting. Therefore, our study used larger tissue blocks, high magnetic field (7T), but a lower resolution (100 μm isotropic) and focussed on the complete cortex. This allowed the identification of patterns of iron-induced contrast changes over the entire cortex rather than focussing on individual $A\beta$ plaques.

We observed an inhomogeneous appearance of the cortex characterized by a granular appearance and foci of signal loss in AD patients. These MRI contrast changes have been previously reported [18–20], but were assigned to represent $A\beta$ plaques [18–20]. The inhomogeneous appearance of the cortex was hypothesized to be caused by smaller plaques containing less iron, thereby causing partial signal loss [19]. Recently, van Bergen et al., 2016 showed increased cortical iron levels, measured by quantitative susceptibility mapping (QSM) MRI, in PiB-positive APOE-ϵ4 carriers with mild cognitive impairment [22]. Complementary work from our lab on post-mortem AD tissue showed that the degree of altered iron accumulation is positively correlated with the amount of $A\beta$ plaques [35]. However, our spatial correlation analysis showed that the observed contrast changes on MRI do not co-localize with the distribution of $A\beta$ plaques in the cortex. This was confirmed by the histological images; $A\beta$ plaques were found in all cortical layers, whereas the MRI contrast changes and iron and myelin changes only cover the middle cortical layers (III/IV), extending till layer II and V. Moreover, although iron was observed in $A\beta$ plaques, significant amounts of iron were also found in myelinated fibers and microglia, showing that iron-induced contrast changes in AD reflect not solely $A\beta$ plaques. Microscopic studies of the hippocampus and entorhinal cortex also confirm that microglia contribute to iron accumulation in AD [36, 37].

The spatial correlations reported in this study demonstrate a relationship between cortical iron accumulation, changes in gray matter myelin, and T_2^*-weighted contrast.

Consistent with our findings, both iron and myelin have been previously suggested as important sources for magnetic susceptibility-based MRI contrast [38–40]. In the human occipital cortex, for example, iron was found to be the dominant source of MRI contrast and laminar variations in iron content were reflected on MRI [38]. Another study, confirmed that T_2^*-weighted tissue contrast is also influenced by myelin [40]. Moreover, the observed co-localization of iron and myelin on both the histological level and on the ultrastructural level using electron microscopy is consistent with earlier observations [31, 38] in normal human brain tissue and is suggested to reflect the role of iron in the synthesis of myelin; to ensure the availability of iron during myelin maintenance and repair, iron is stored in ferritin deposits close the myelination sites [41]. In our study, we demonstrate that in AD, a high proportion of iron is still associated with myelin, as was also demonstrated by Quintana et al. [31]. This indicates that both in the healthy brain and in disease, MRI reflects the underlying myelin cytoarchitecture. This is particularly interesting as the pathophysiology of AD is still not fully understood; an excess of iron caused by ferritin dysfunctioning and myelin dyshomeostasis have both been proposed as mechanisms underlying AD [31, 42].

Our data confirm that iron and myelin are important sources for T_2^*-weighted MRI contrast, but even more importantly, we show that the cortical iron distribution and myelin architecture is disturbed in AD patients. Although $A\beta$ and neurofibrillary tau degeneration are considered as key mediators of AD, disturbed homeostasis of both iron and myelin is increasingly reported as potential factors contributing to AD pathophysiology [11–13, 21]. Nonetheless, changes in cortical myelin have only rarely been reported. Focal demyelination around $A\beta$ plaques has been mentioned [43], but we observed a disturbed cortical myelin architecture and an increased myelin staining not spatially related to $A\beta$ plaques. One other study, using an amyloidosis mouse model, observed similar cortical myelin changes [44]. This study showed a severely disorganized cortical myelin architecture in old $A\beta$ overproducing APP/PS1 transgenic mice; this disruption was dependent of $A\beta$ load. This is consistent with our findings, with cortical myelin architecture showing the most striking changes in the EOAD group. Although little is known about the relation between AD pathology and white matter, a recent in vivo MRI study by Dean et al., showed that amyloid pathologies, measured by CSF, significantly influences white matter and that this might be a feature early in the disease process [45].

Although the reported results suggest an increase of myelin, it is not known what the origin is of these changes. It might be possible that the number of myelinated fibers is changed or that the amount of myelination per fiber is increased. On the other hand, an increased staining intensity does not necessarily mean more protein; epitope availability might affect the staining. Quantitative measurements of myelin, with for example mass spectrometry, are needed to give more insight. Thirdly, it is possible that the increased myelin density and the collapse of structural integrity is the result of cortical

compaction due to cortical atrophy and loss of neurons and supporting cells. However, measuring atrophy was not possible in our post-mortem samples since we used small tissue blocks and deformation due to formalin fixation might be present. Moreover, normal variation in cortical thickness is present over the brain. Therefore, in vivo or in situ post-mortem scans should link our iron-based MRI scans to local cortical atrophy.

Apart from differences between AD patients and control subjects, we also observed differences between LOAD and EOAD patients. Overall, the EOAD patients were more affected on both MRI and histology. Our findings are consistent with the previously reported higher cortical phase changes on MRI in EOAD patients, and confirm that these phase changes can indeed be interpreted as a result of increased cortical iron load [23]. Previous histological studies on LOAD and EOAD patients demonstrated larger amounts of $A\beta$ plaques and neurofibrillary tangles in EOAD patients [7], which we also found in our study. However, histological differences in iron accumulation between LOAD and EOAD patients have not previously been reported. Although it is in general suggested that AD patients have increased iron accumulation, conflicting results depending on study population, measurement method and brain region have been reported [21, 46, 47]. Future high-field MRI studies using, for example, QSM are needed to give more insight into the spatial localization and increase of iron in AD.

Neuro-inflammation is recognized as another important factor in AD pathophysiology and generally thought to be initially caused by recruitment of activated astrocytes and microglia to $A\beta$ plaques [48]. Since $A\beta$ plaque load has been reported to be higher in EOAD patients [7], and both microglia and astrocytes are involved in iron homeostasis [12], neuro-inflammation could partially explain the differences found in iron accumulation between LOAD and EOAD patients. Previous studies have shown an association between inflammation, atrophy and disease progression in AD patients [49, 50]. Moreover, Kreisl et al., 2013 showed that EOAD patients have more inflammation compared to LOAD patients. Therefore, we hypothesize that a pro-inflammatory environment in EOAD patients might lead to an increase of iron-laden microglia and thus increased iron accumulation.

Consistent with previous studies [18, 19], we found an abnormal appearance of the cortex on MRI more frequently in the AD patients compared to control subjects. However, two EOAD patients showed a normal cortical appearance on MRI. Both a MRI scan of an adjacent tissue block as a MRI of a frozen tissue block confirmed these findings and thereby excluded leakage of iron as a cause. Examination of the clinical history revealed that one of these two patients had an APP genomic duplication and that the other patient had an unusual parietal AD phenotype. Clinically it is increasingly recognized that AD is a heterogeneous disease with multiple underlying mechanistic causes and this might explain the variety observed in our study.

Finally, APOE gene status is an important risk factor for AD. Recent studies showed

that the APOE-ϵ4 status is linked to ferritin [16, 22]. More specifically, Ayton et al. 2015 showed that ferritin is strongly associated with CSF ApoE levels and elevated in APOE-ϵ4 carriers [16]. Van Bergen et al., 2016 showed the same association in mild cognitive impairment subjects; significantly higher levels of magnetic susceptibility were found in APOE-ϵ4 carriers [22]. These results suggest that the APOE-ϵ4 allele may increase the risk of developing AD via brain iron accumulation, possibly due to reduced clearance of iron because of the low affinity of APOE-ϵ4 to high-density lipoprotein [16]. In our study, APOE gene status was determined for 29/34 subjects, but our sample size is too small to make a definitive conclusion. Moreover, the LOAD group included by chance significantly more APOE-ϵ4 carriers compared to the control group, but very few non-APOE-ϵ4 carriers. In EOAD patients no clear differences were found between APOE-ϵ4 carriers and non-carriers, but other genetic risk factors as APP or PSEN1 mutations might be present in this sample population as well. Besides APOE status, mutations in iron-regulating genes, such as the HFE gene, are also known to be implicated in brain iron accumulation and AD age of onset [17]. Future studies correlating iron-related genetic variants to the cortical appearance on MRI would be of interest.

A limitation of this study is the use of a semi-quantitative scoring system for both histology and MRI instead of a quantitative approach. However, quantitative approaches to measure histological staining intensity are predominately based on contrast. In our study, we scored the presence of a band-shaped increased staining intensity which is difficult to quantify using image analyses since it is not merely an increased intensity but a different distribution of iron and myelin. Also for MRI, we scored for a change in distribution rather than an increase of contrast. A quantitative approach to extract these cortical features is texture analysis which provides quantitative means to describe tissue heterogeneity, as has been shown by Hwang et al. This study showed that QSM texture analyses can be used to distinguish both MCI and AD patients from controls [51]. Although we used a semi-quantitative scoring system to differentiate between controls, LOAD and EOAD patients, our conclusion that these differences are best explained by changes in iron and myelin were based on quantitative measurements. The pixel-by-pixel correlation analysis is done on the pixel intensities of both MRI and histology and therefor fully quantitative.

In conclusion, on ultra-high field MRI control subjects, LOAD patients and EOAD patients had a different appearance of the cerebral frontal cortex. These MRI contrast changes are best explained by cortical iron accumulation and changes in myelin organization, whereas amyloid and tau showed less spatial correspondence. MRI measurements of iron could play a crucial role in classifying subtypes of AD for further mechanistic studies.

ACKNOWLEDGMENTS

The authors thank I. M. Hegeman-Kleinn for her technical assistance and J. J. Goeman for his advice on the statistical analyses. This work was supported by a project grant from the EU Seventh Framework Programme: FP7-PEOPLE-2013-IAPP (612360 – BRAINPATH)

SUPPLEMENTARY TABLES AND FIGURES

Staining	Primary Antibody	Dilution	Pre-treatment	Counterstaining
Aβ	Anti-human *Aβ* (6F/3D, DakoCytomation, Glostrup, Denmark)	1:20	Formic acid (1 hour) + Trypsin (30 minutes at 37°C)	Harris Haematoxylin
Astrocytes	Anti-human GFAP monoclonal mouse (6F2, DakoCytomation, Glostrup, Denmark)	1:1000	Boiled in citrate buffer (20 minutes, pH 6)	Harris Haematoxylin
Microglia	Anti-human CD68 monoclonal mouse (KP1, DakoCytomation, Glostrup, Denmark)	1:50	Boiled in citrate buffer (20 minutes, pH 6)	Harris Haematoxylin
Myelin	Anti-proteolipid protein (PLP) monoclonal mouse (Serotec)	1:1000	N.A.	N.A.
Tau	Anti-PHF-tau monoclonal mouse (AT8, Innogenetics, Ghent, Belgium)	1:2000	N.A.	Harris Haematoxylin

Table S1: **Immunohistochemistry details including primary and secondary antibodies and additional pre-treatments.** Secondary Antibody: Biotinylated rabbit anti-mouse, 1:200, (DakoCytomation, Glostrup, Denmark) followed by ABC (Vector) and DAB.

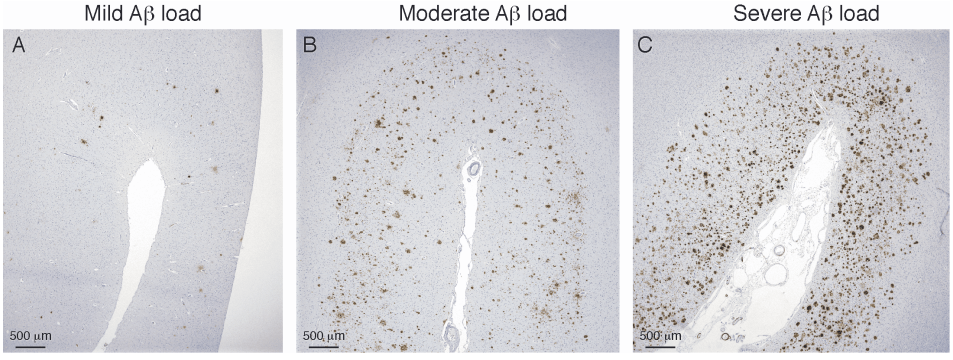

Figure S1: **Histology examples of the *Aβ* plaque load scoring.** *Aβ* plaque load was scored as: mild, moderate or severe.

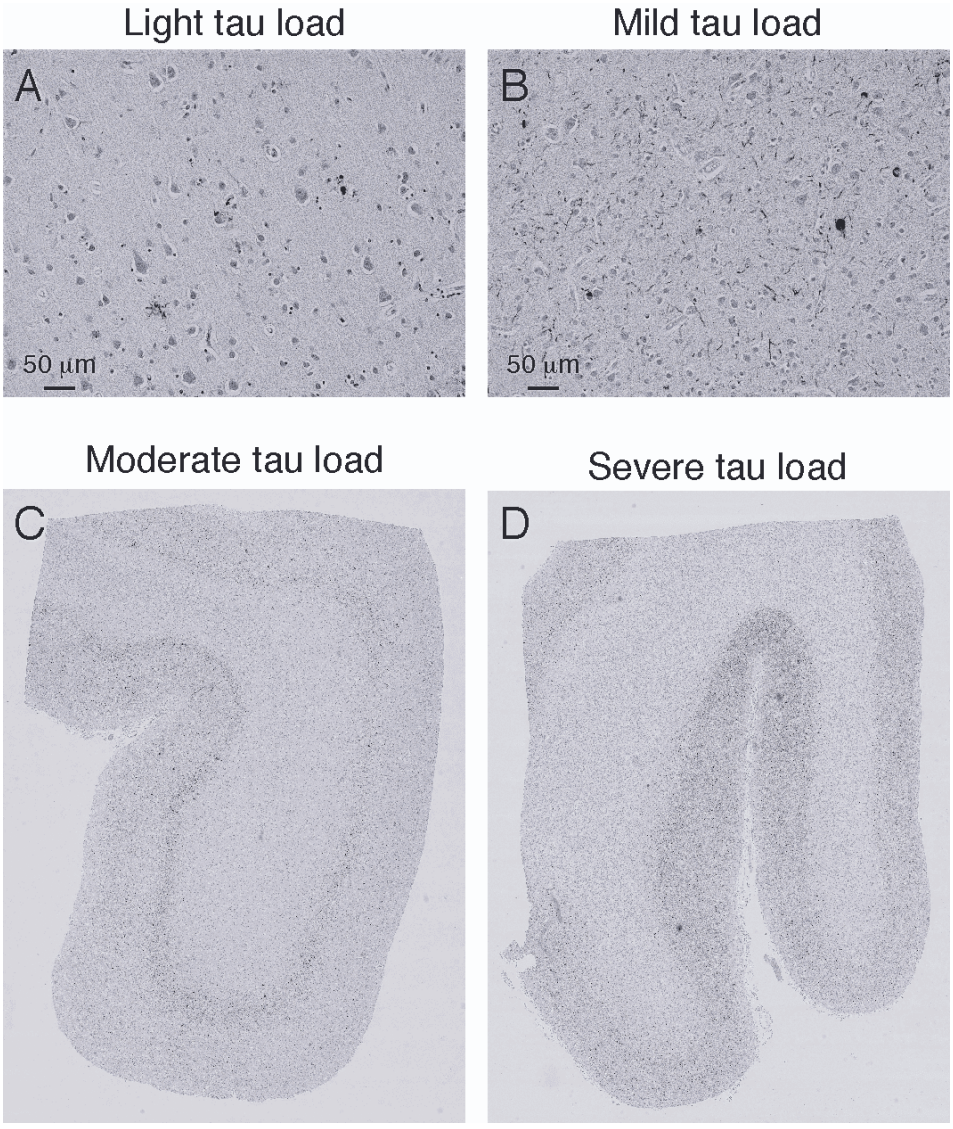

Figure S2: **Histology examples of the tau load scoring.** Tau load was scored as: light, mild, moderate or severe. The used scoring system was based on our own observations and adapted from Alafuzoff et al., 2008, with categories ranging from light tau load till severe tau load. The last two categories (moderate and severe) are macroscopically instead of microscopically determined by exploring the complete cortical ribbon.

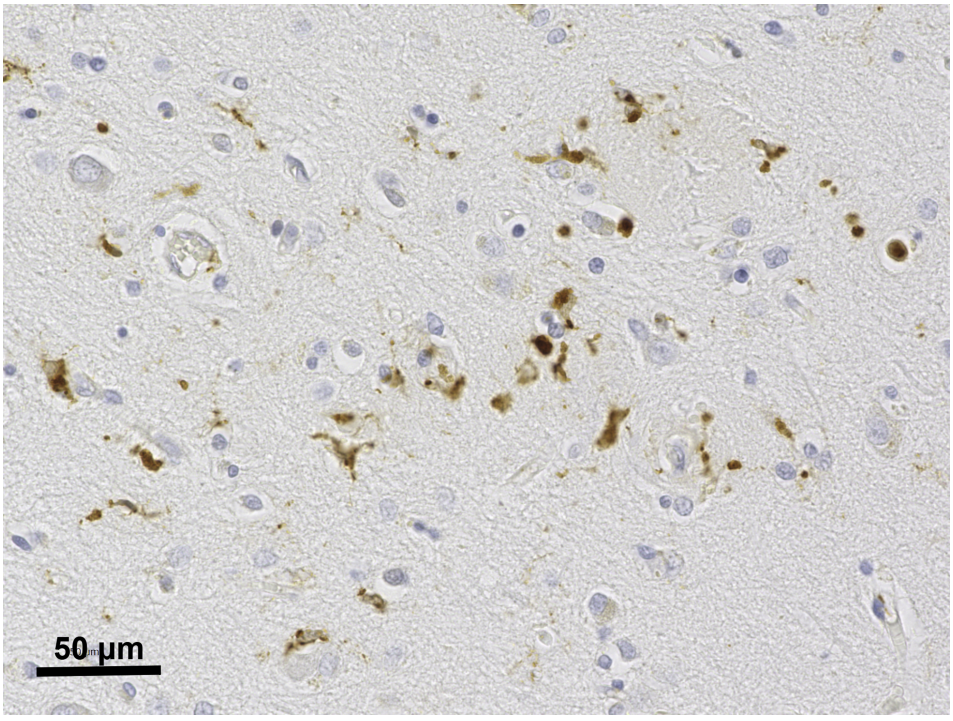

Figure S3: **High resolution and zoomed image of a microglia observed in the cortex.**

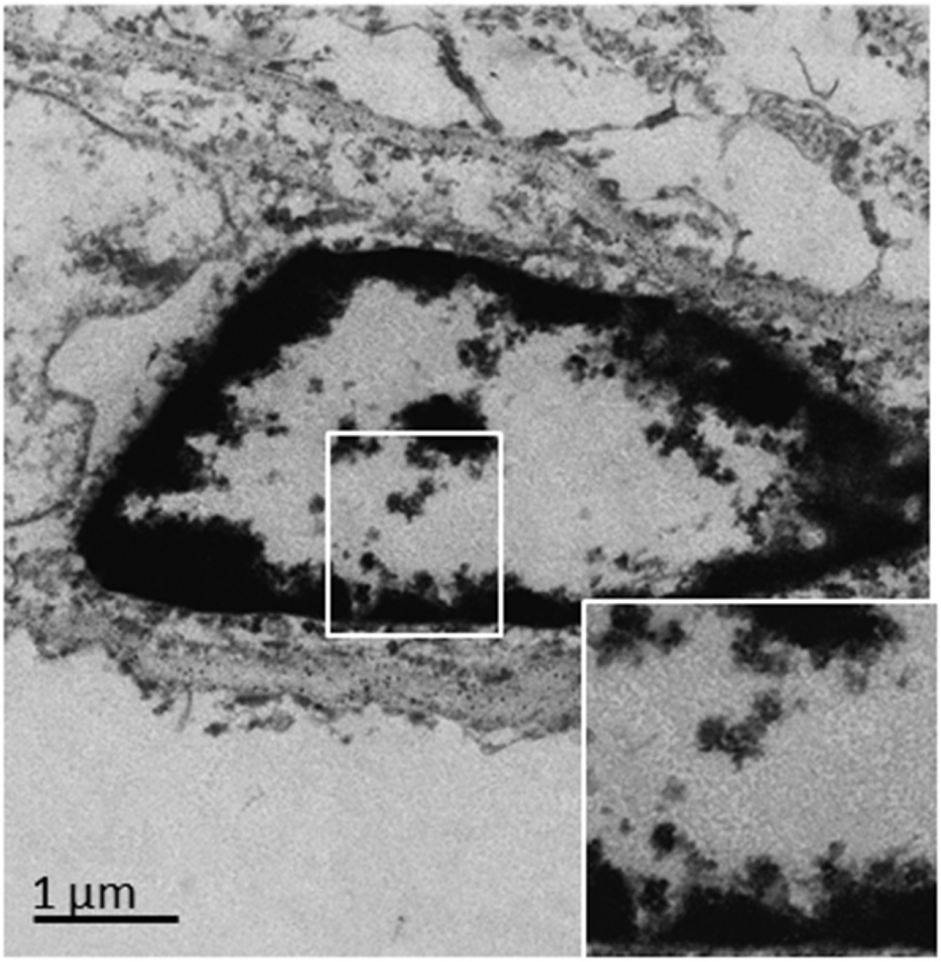

Figure S4: **Electron microscopy image of an endothelial cell observed in an EOAD patients.** Cells with the morphological traits of endothelial cells show no to little iron.

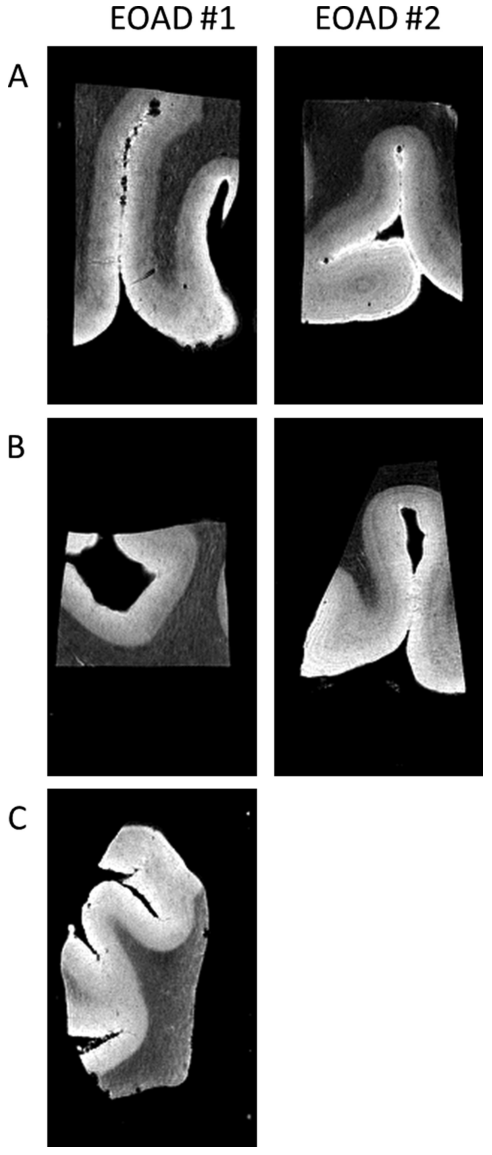

Figure S5: **MRI scans of two EOAD patients with a normal cortical appearance on MRI.** (A) The frontal cortex of both patients was normal as indicated by a low total MRI score. (B) This observation was confirmed by an adjacent tissue block showing the same cortical appearance. (C) Leakage of iron was excluded by scanning a frozen tissue block, same brain region, of EOAD patient #1 which was thawed in formalin and fixed for three days at room temperature. Also this MRI scan showed a normal cortical appearance.

BIBLIOGRAPHY

[1] C. Reitz and R. Mayeux, *Alzheimer disease: epidemiology, diagnostic criteria, risk factors and biomarkers,* Biochem Pharmacol **88**, 640 (2014).

[2] W. M. van der Flier, Y. A. Pijnenburg, N. C. Fox, and P. Scheltens, *Early-onset versus late-onset alzheimer's disease: the case of the missing apoe varepsilon4 allele,* Lancet Neurol **10**, 280 (2011).

[3] Alzheimer'sAssociation, *2016 alzheimer's disease facts and figures,* Alzheimers Dement **12**, 459 (2016).

[4] E. Koss, S. Edland, G. Fillenbaum, R. Mohs, C. Clark, D. Galasko, and J. C. Morris, *Clinical and neuropsychological differences between patients with earlier and later onset of alzheimer's disease: A cerad analysis .12.* Neurology **46**, 136 (1996).

[5] A. E. van der Vlies, E. L. Koedam, Y. A. Pijnenburg, J. W. Twisk, P. Scheltens, and W. M. van der Flier, *Most rapid cognitive decline in apoe epsilon4 negative alzheimer's disease with early onset,* Psychol Med **39**, 1907 (2009).

[6] H. Cho, S. W. Seo, J. H. Kim, M. K. Suh, J. H. Lee, Y. S. Choe, K. H. Lee, J. S. Kim, G. H. Kim, Y. Noh, B. S. Ye, H. J. Kim, C. W. Yoon, J. Chin, and D. L. Na, *Amyloid deposition in early onset versus late onset alzheimer's disease,* J Alzheimers Dis **35**, 813 (2013).

[7] G. A. Marshall, L. A. Fairbanks, S. Tekin, H. V. Vinters, and J. L. Cummings, *Early-onset alzheimer's disease is associated with greater pathologic burden,* J Geriatr Psychiatry Neurol **20**, 29 (2007).

[8] S. Palmqvist, H. Zetterberg, K. Blennow, S. Vestberg, U. Andreasson, D. J. Brooks, R. Owenius, D. Hagerstrom, P. Wollmer, L. Minthon, and O. Hansson, *Accuracy of brain amyloid detection in clinical practice using cerebrospinal fluid beta-amyloid 42: a cross-validation study against amyloid positron emission tomography,* JAMA Neurol **71**, 1282 (2014).

[9] M. Sauvee, G. DidierLaurent, C. Latarche, M. C. Escanye, J. L. Olivier, and C. Malaplate-Armand, *Additional use of abeta(4)(2)/abeta(4)(0) ratio with cerebrospinal fluid biomarkers p-tau and abeta(4)(2) increases the level of evidence of alzheimer's disease pathophysiological process in routine practice,* J Alzheimers Dis **41**, 377 (2014).

[10] T. J. Montine, C. H. Phelps, T. G. Beach, E. H. Bigio, N. J. Cairns, D. W. Dickson, C. Duyckaerts, M. P. Frosch, E. Masliah, S. S. Mirra, P. T. Nelson, J. A. Schneider, D. R. Thal, J. Q. Trojanowski, H. V. Vinters, and B. T. Hyman, *National institute on aging-alzheimer's association guidelines for the neuropathologic assessment of alzheimer's disease: a practical approach,* Acta Neuropathol **123**, 1 (2012).

[11] D. Hare, S. Ayton, A. Bush, and P. Lei, *A delicate balance: Iron metabolism and diseases of the brain,* Front Aging Neurosci **5**, 34 (2013).

[12] D. G. Peters, J. R. Connor, and M. D. Meadowcroft, *The relationship between iron dyshomeostasis and amyloidogenesis in alzheimer's disease: Two sides of the same coin,* Neurobiol Dis **81**, 49 (2015).

[13] R. J. Ward, F. A. Zucca, J. H. Duyn, R. R. Crichton, and L. Zecca, *The role of iron in brain ageing and neurodegenerative disorders,* Lancet Neurol **13**, 1045 (2014).

[14] L. Zecca, M. B. Youdim, P. Riederer, J. R. Connor, and R. R. Crichton, *Iron, brain ageing and neurodegenerative disorders,* Nat Rev Neurosci **5**, 863 (2004).

[15] L. Silvestri, A. Pagani, and C. Camaschella, *Furin-mediated release of soluble hemojuvelin: a new link between hypoxia and iron homeostasis,* Blood **111**, 924 (2008).

[16] S. Ayton, N. G. Faux, A. I. Bush, and I. Alzheimer's Disease Neuroimaging, *Ferritin levels in the cerebrospinal fluid predict alzheimer's disease outcomes and are regulated by apoe,* Nat Commun **6**, 6760 (2015).

[17] F. Ali-Rahmani, C. L. Schengrund, and J. R. Connor, *Hfe gene variants, iron, and lipids: a novel connection in alzheimer's disease,* Front Pharmacol **5**, 165 (2014).

[18] R. J. Nabuurs, I. Hegeman, R. Natte, S. G. van Duinen, M. A. van Buchem, L. van der Weerd, and A. G. Webb, *High-field mri of single histological slices using an inductively coupled, self-resonant microcoil: application to ex vivo samples of patients with alzheimer's disease,* NMR Biomed **24**, 351 (2011).

[19] S. van Rooden, M. L. Maat-Schieman, R. J. Nabuurs, L. van der Weerd, S. van Duijn, S. G. van Duinen, R. Natte, M. A. van Buchem, and J. van der Grond, *Cerebral amyloidosis: postmortem detection with human 7.0-t mr imaging system,* Radiology **253**, 788 (2009).

[20] R. J. Nabuurs, R. Natte, F. M. de Ronde, I. Hegeman-Kleinn, J. Dijkstra, S. G. van Duinen, A. G. Webb, A. J. Rozemuller, M. A. van Buchem, and L. van der Weerd, *Mr microscopy of human amyloid-beta deposits: characterization of parenchymal amyloid, diffuse plaques, and vascular amyloid,* J Alzheimers Dis **34**, 1037 (2013).

[21] S. van Rooden, M. J. Versluis, M. K. Liem, J. Milles, A. B. Maier, A. M. Oleksik, A. G. Webb, M. A. van Buchem, and J. van der Grond, *Cortical phase changes in alzheimer's disease at 7t mri: a novel imaging marker,* Alzheimers Dement **10**, e19 (2014).

[22] J. M. van Bergen, X. Li, J. Hua, S. J. Schreiner, S. C. Steininger, F. C. Quevenco, M. Wyss, A. F. Gietl, V. Treyer, S. E. Leh, F. Buck, R. M. Nitsch, K. P. Pruessmann,

P. C. van Zijl, C. Hock, and P. G. Unschuld, *Colocalization of cerebral iron with amyloid beta in mild cognitive impairment,* Sci Rep **6**, 35514 (2016).

[23] S. van Rooden, N. T. Doan, M. J. Versluis, J. D. Goos, A. G. Webb, A. M. Oleksik, W. M. van der Flier, P. Scheltens, F. Barkhof, A. W. Weverling-Rynsburger, G. J. Blauw, J. H. Reiber, M. A. van Buchem, J. Milles, and J. van der Grond, *7t t(2)*-weighted magnetic resonance imaging reveals cortical phase differences between early- and late-onset alzheimer's disease,* Neurobiol Aging **36**, 20 (2015).

[24] S. van Duijn, R. J. Nabuurs, S. van Rooden, M. L. Maat-Schieman, S. G. van Duinen, M. A. van Buchem, L. van der Weerd, and R. Natte, *Mri artifacts in human brain tissue after prolonged formalin storage,* Magn Reson Med **65**, 1750 (2011).

[25] T. M. Shepherd, P. E. Thelwall, G. J. Stanisz, and S. J. Blackband, *Aldehyde fixative solutions alter the water relaxation and diffusion properties of nervous tissue,* Magn Reson Med **62**, 26 (2009).

[26] H. Braak, E. Braak, and P. Kalus, *Alzheimer's disease: areal and laminar pathology in the occipital isocortex,* Acta Neuropathol **77**, 494 (1989).

[27] R. Meguro, Y. Asano, S. Odagiri, C. Li, H. Iwatsuki, and K. Shoumura, *Nonheme-iron histochemistry for light and electron microscopy: a historical, theoretical and technical review,* Arch Histol Cytol **70**, 1 (2007).

[28] S. van Duijn, R. J. Nabuurs, S. G. van Duinen, and R. Natte, *Comparison of histological techniques to visualize iron in paraffin-embedded brain tissue of patients with alzheimer's disease,* J Histochem Cytochem **61**, 785 (2013).

[29] W. M. Abdelmoula, R. J. Carreira, R. Shyti, B. Balluff, R. J. van Zeijl, E. A. Tolner, B. F. Lelieveldt, A. M. van den Maagdenberg, L. A. McDonnell, and J. Dijkstra, *Automatic registration of mass spectrometry imaging data sets to the allen brain atlas,* Anal Chem **86**, 3947 (2014).

[30] S. R. Aylward and E. Bullitt, *Initialization, noise, singularities, and scale in height ridge traversal for tubular object centerline extraction,* IEEE Trans Med Imaging **21**, 61 (2002).

[31] C. Quintana, S. Bellefqih, J. Y. Laval, J. L. Guerquin-Kern, T. D. Wu, J. Avila, I. Ferrer, R. Arranz, and C. Patino, *Study of the localization of iron, ferritin, and hemosiderin in alzheimer's disease hippocampus by analytical microscopy at the subcellular level,* J Struct Biol **153**, 42 (2006).

[32] X. B. Liu and C. M. Schumann, *Optimization of electron microscopy for human brains with long-term fixation and fixed-frozen sections,* Acta Neuropathol Commun **2**, 42 (2014).

[33] A. Peters and C. Folger, *A website entitled "the fine structure of the aging brain",* J Comp Neurol **521**, 1203 (2013).

[34] M. D. Meadowcroft, J. R. Connor, M. B. Smith, and Q. X. Yang, *Mri and histological analysis of beta-amyloid plaques in both human alzheimer's disease and app/ps1 transgenic mice,* J Magn Reson Imaging **29**, 997 (2009).

[35] S. van Duijn, M. Bulk, S. G. van Duinen, R. J. Nabuurs, M. A. van Buchem, L. van der Weerd, and R. Natte, *Cortical iron reflects severity of alzheimer disease,* Journal of Alzheimer's Disease **In press** (2017).

[36] M. D. Meadowcroft, J. R. Connor, and Q. X. Yang, *Cortical iron regulation and inflammatory response in alzheimer's disease and appswe/ps1deltae9 mice: a histological perspective,* Front Neurosci **9**, 255 (2015).

[37] M. M. Zeineh, Y. Chen, H. H. Kitzler, R. Hammond, H. Vogel, and B. K. Rutt, *Activated iron-containing microglia in the human hippocampus identified by magnetic resonance imaging in alzheimer disease,* Neurobiol Aging **36**, 2483 (2015).

[38] M. Fukunaga, T. Q. Li, P. van Gelderen, J. A. de Zwart, K. Shmueli, B. Yao, J. Lee, D. Maric, M. A. Aronova, G. Zhang, R. D. Leapman, J. F. Schenck, H. Merkle, and J. H. Duyn, *Layer-specific variation of iron content in cerebral cortex as a source of mri contrast,* Proc Natl Acad Sci U S A **107**, 3834 (2010).

[39] C. Langkammer, N. Krebs, W. Goessler, E. Scheurer, F. Ebner, K. Yen, F. Fazekas, and S. Ropele, *Quantitative mr imaging of brain iron: a postmortem validation study,* Radiology **257**, 455 (2010).

[40] M. N. Wallace, M. J. Cronin, R. W. Bowtell, I. S. Scott, A. R. Palmer, and P. A. Gowland, *Histological basis of laminar mri patterns in high resolution images of fixed human auditory cortex,* Front Neurosci **10**, 455 (2016).

[41] B. Todorich, J. M. Pasquini, C. I. Garcia, P. M. Paez, and J. R. Connor, *Oligodendrocytes and myelination: the role of iron,* Glia **57**, 467 (2009).

[42] G. Bartzokis, *Alzheimer's disease as homeostatic responses to age-related myelin breakdown,* Neurobiol Aging **32**, 1341 (2011).

[43] S. Mitew, M. T. Kirkcaldie, G. M. Halliday, C. E. Shepherd, J. C. Vickers, and T. C. Dickson, *Focal demyelination in alzheimer's disease and transgenic mouse models,* Acta Neuropathol **119**, 567 (2010).

[44] H. Chen, S. Epelbaum, and B. Delatour, *Fiber tracts anomalies in appxps1 transgenic mice modeling alzheimer's disease,* J Aging Res **2011**, 281274 (2011).

[45] r. Dean, D. C., S. A. Hurley, S. R. Kecskemeti, J. P. O'Grady, C. Canda, N. J. Davenport-Sis, C. M. Carlsson, H. Zetterberg, K. Blennow, S. Asthana, M. A. Sager, S. C. Johnson, A. L. Alexander, and B. B. Bendlin, *Association of amyloid pathology with myelin alteration in preclinical alzheimer disease,* JAMA Neurol **74**, 41 (2017).

[46] Z. Luo, X. Zhuang, D. Kumar, X. Wu, C. Yue, C. Han, and J. Lv, *The correlation of hippocampal t2-mapping with neuropsychology test in patients with alzheimer's disease,* PLoS One **8**, e76203 (2013).

[47] D. J. Hare, E. P. Raven, B. R. Roberts, M. Bogeski, S. D. Portbury, C. A. McLean, C. L. Masters, J. R. Connor, A. I. Bush, P. J. Crouch, and P. A. Doble, *Laser ablation-inductively coupled plasma-mass spectrometry imaging of white and gray matter iron distribution in alzheimer's disease frontal cortex,* Neuroimage **137**, 124 (2016).

[48] M. T. Heneka, M. J. Carson, J. El Khoury, G. E. Landreth, F. Brosseron, D. L. Feinstein, A. H. Jacobs, T. Wyss-Coray, J. Vitorica, R. M. Ransohoff, K. Herrup, S. A. Frautschy, B. Finsen, G. C. Brown, A. Verkhratsky, K. Yamanaka, J. Koistinaho, E. Latz, A. Halle, G. C. Petzold, T. Town, D. Morgan, M. L. Shinohara, V. H. Perry, C. Holmes, N. G. Bazan, D. J. Brooks, S. Hunot, B. Joseph, N. Deigendesch, O. Garaschuk, E. Boddeke, C. A. Dinarello, J. C. Breitner, G. M. Cole, D. T. Golenbock, and M. P. Kummer, *Neuroinflammation in alzheimer's disease,* Lancet Neurol **14**, 388 (2015).

[49] R. Leung, P. Proitsi, A. Simmons, K. Lunnon, A. Guntert, D. Kronenberg, M. Pritchard, M. Tsolaki, P. Mecocci, I. Kloszewska, B. Vellas, H. Soininen, L. O. Wahlund, and S. Lovestone, *Inflammatory proteins in plasma are associated with severity of alzheimer's disease,* PLoS One **8**, e64971 (2013).

[50] W. C. Kreisl, C. H. Lyoo, M. McGwier, J. Snow, K. J. Jenko, N. Kimura, W. Corona, C. L. Morse, S. S. Zoghbi, V. W. Pike, F. J. McMahon, R. S. Turner, R. B. Innis, and P. E. T. R. P. T. Biomarkers Consortium, *In vivo radioligand binding to translocator protein correlates with severity of alzheimer's disease,* Brain **136**, 2228 (2013).

[51] E. J. Hwang, H. G. Kim, D. Kim, H. Y. Rhee, C. W. Ryu, T. Liu, Y. Wang, and G. H. Jahng, *Texture analyses of quantitative susceptibility maps to differentiate alzheimer's disease from cognitive normal and mild cognitive impairment,* Med Phys **43**, 4718 (2016).